

# Influence of Pyrrhotite on the Corrosion of Mild Steel

Saba Navabzadeh Esmaeely,<sup>‡,\*</sup> Gheorghe Bota,<sup>\*</sup> Bruce Brown,<sup>\*</sup> and Srdjan Nešić<sup>\*</sup>

## ABSTRACT

As a result of the electrical conductivity of pyrrhotite, it was hypothesized that its presence in the corrosion product layer on a steel surface could lead to localized corrosion. Mild steel specimens (API 5L X65) were pretreated to form a pyrrhotite layer on the surface using high-temperature sulfidation in oil. The pretreated specimens were then exposed to a range of aqueous CO<sub>2</sub> and H<sub>2</sub>S corrosion environments at 30°C and 60°C. X-ray diffraction data showed that the pyrrhotite layer changed during exposure; in an aqueous CO<sub>2</sub> solution it underwent dissolution, while in a mixed CO<sub>2</sub>/H<sub>2</sub>S solution it partially transformed to troilite, with some mackinawite formation. Initiation of localized corrosion was observed in both cases. It was concluded that this was the result of a galvanic coupling between the pyrrhotite layer and the steel surface. The intensity of the observed localized corrosion varied with solution conductivity (NaCl concentration); a more conductive solution resulted in higher localized corrosion rates, consistent with the galvanic nature of the attack.

**KEY WORDS:** CO<sub>2</sub>, H<sub>2</sub>S corrosion, localized corrosion, pyrrhotite, troilite, x-ray diffraction

## INTRODUCTION

In H<sub>2</sub>S-containing environments encountered in the oil and gas industry, localized corrosion is a potential cause leading to facility failure. There can be a high

rate of metal loss in a very limited area, which may be covered by a corrosion product layer. This makes H<sub>2</sub>S localized corrosion more difficult to predict and detect prior to failure by using the conventional corrosion inspection and monitoring methods.<sup>1-2</sup> Considering the often random spatial distribution of localized attack and the limited number of monitoring probes that can be installed in any given facility, the chances of detecting localized corrosion this way are slim at best. Internal line inspection techniques that could theoretically detect localized attack are complicated, expensive, and therefore are used infrequently. Thus, a better understanding of localized corrosion mechanisms would be essential for the development of predictive models and implementation of corrosion mitigation strategies.

There are complicating factors associated with the investigation of H<sub>2</sub>S corrosion mechanisms. This includes the recently found electrochemical mechanisms involving direct reduction of H<sub>2</sub>S at the metal surface<sup>3-5</sup> and the role of different iron sulfides<sup>6-12</sup> that can form on the metal surface in the corrosion process. In H<sub>2</sub>S solutions, the corrosion product layer can be composed of various iron sulfides with distinct physicochemical and electrical properties.<sup>13-18</sup> The electrical conductivity of various iron sulfides is one of the key parameters. For example, pyrrhotite (Fe<sub>1-x</sub>S), troilite (FeS), and pyrite (FeS<sub>2</sub>) all occur as stable corrosion products and have similar electrical conductivities,<sup>13-15</sup> while for the more unstable mackinawite (FeS) there are far fewer values reported for its conductivity.<sup>19</sup> Mackinawite has anisotropic electrical properties, being conductive in

Submitted for publication: May 8, 2017. Revised and accepted: June 10, 2017. Preprint available online: July 17, 2017, <http://dx.doi.org/10.5006/2505>.

<sup>‡</sup> Corresponding author. E-mail: [sn294410@ohio.edu](mailto:sn294410@ohio.edu).

<sup>\*</sup> Institute for Corrosion and Multiphase Flow Technology, Department of Chemical and Biomolecular Engineering, Ohio University, Athens, OH 45701.

the direction of oriented layers in its crystal structure and much less conductive in the perpendicular direction.<sup>19</sup> The existence of conductive phases on a steel surface significantly impacts the electrochemically driven corrosion process.<sup>3,20-21</sup> The conductive corrosion product layer may intensify the electrochemical reaction rate by providing a larger cathodic surface area, locally or uniformly across the corroding steel surface.

Localized H<sub>2</sub>S corrosion in electrolytes, typically an aqueous NaCl solution, has been attributed to three main reasons: the presence of elemental sulfur,<sup>22-25</sup> partial formation/failure of the iron sulfide corrosion product layer,<sup>26</sup> and formation of multiple iron sulfide polymorphs in a corrosion product layer, leading to non-uniform electrical conductivity.<sup>27-29</sup> Over the past decade, the role of conductive iron sulfides on localized corrosion in H<sub>2</sub>S saturated aqueous solutions has become a focus area for corrosion scientists.<sup>27-32</sup> However, the research has not yielded decisive insights into the mechanisms and the possible role of different conductive iron sulfides.<sup>27-29</sup>

Several studies on corrosion of mild steel in H<sub>2</sub>S/CO<sub>2</sub> gas mixtures have been conducted where experiments involved investigation of multiple parameters including the effect of pH and glycol.<sup>28,32-38</sup> In a recent study, Kvarckvål, et al.,<sup>28</sup> reported intensified uniform and localized corrosion rates under a pyrrhotite/troilite layer in the presence of a conductive electrolyte. However, as a result of the complexity of their experimental conditions, the corrosion mechanisms related to the observed localized corrosion remained unclear.

As for the role of conductive corrosion product layers on localized corrosion, Ning, et al.,<sup>27</sup> demonstrated that a mild steel surface could undergo localized corrosion when in direct contact with pyrite, in the presence of a corrosive electrolyte. They proposed that localized corrosion takes place as a result of galvanic coupling between pyrite and the steel. This was attributed to pyrite being conductive, hence forming a galvanic cell with the exposed part of the steel surface. However, the authors did not report localized corrosion in the presence of pyrrhotite/troilite. Considering that pyrrhotite/troilite are in a similar conductivity range as pyrite, one can expect that they could also act as a driving force for localized corrosion<sup>13-15</sup> (Table 1). Furthermore, they all have a similar open-circuit potential (OCP), much more positive than mild steel<sup>39-41</sup> (Table 1). Hypothetically, when in contact with a mild steel surface, all of them could act as a cathode and lead to an increase in the corrosion rate through a galvanic effect.<sup>42</sup>

There are earlier studies that addressed this problem. Adam, et al.,<sup>43</sup> investigated the galvanic coupling of pyrrhotite with various steels and reported a larger potential difference and a higher current between the pyrrhotite and mild steel as compared to other

**TABLE 1**  
*Iron Sulfide Properties*

Material	Resistivity <sup>13-15</sup>	OCP in a Deoxygenated Solution at pH 4.0 vs. sat. Ag/AgCl <sup>39-41</sup>
Mild steel	$\leq 10^{-8}$ Ω·m	from -0.65 to -0.7 V
Pyrite	$10^{-5}$ to $10$ Ω·m	from 0.16 to -0.22 V
Pyrrhotite	$10^{-6}$ to $0.1$ Ω·m	from -0.08 to -0.22 V
Troilite	$10^{-6}$ to $0.1$ Ω·m	

types of galvanic couples. The authors reported a higher galvanic current at lower pH where the mild steel is not passivated. Pyrrhotite<sup>44</sup> and pyrite<sup>45</sup> are reported to be good electro-catalysts for the hydrogen evolution reaction. Thus, it appears that if the steel is coupled with one or both of these iron sulfides in a conductive acidic media, higher corrosion rates would be observed, either locally or uniformly due to an increase in cathodic surface area.<sup>46</sup>

While there seems to be evidence of the role of pyrite in localized corrosion,<sup>27</sup> contradictory reports are found with respect to the role of pyrrhotite/troilite,<sup>27-28</sup> which motivated the current study. Here, the focus is on galvanic coupling of a pyrrhotite/troilite layer with the steel underneath. Initial experiments were conducted in an aqueous electrolyte saturated with CO<sub>2</sub>, followed by experiments in an H<sub>2</sub>S-saturated electrolyte, and finally a mixed CO<sub>2</sub>/H<sub>2</sub>S electrolyte was used. The experiments in an aqueous CO<sub>2</sub> solution were conducted first, for several reasons: (i) they are much simpler and provide a good training opportunity where most of the experimental problems and analyses could be worked out before moving the experimentation into an H<sub>2</sub>S environment, which is much more challenging; (ii) the galvanic coupling between the pyrrhotite layer and the steel surface was present in both environments; and (iii) in order to study the behavior in a mixed CO<sub>2</sub>/H<sub>2</sub>S environment which is most realistic for field applications, it was beneficial to work with "pure" environments first. Ultimately, this approach provided valuable insights into the behavior of pyrrhotite on the steel surface and enabled the deciphering of the complicated interactions between the steel, the pyrrhotite layer, and the corrosive environment.

## EXPERIMENTAL METHODS

### *Experimental Setup (Electrochemical Measurements)*

Electrochemical experiments were conducted in a conventional three-electrode glass cell, following the experimental matrix described in Table 2. In this setup, the cell was filled with 2 L of deionized (DI) water and 20.2 g of sodium chloride (NaCl) to obtain a 1.0 wt% NaCl electrolyte. The temperature was maintained at 30°C. Electrochemical measurements

**TABLE 2**  
*Test Matrix*

Parameters	Conditions
Total pressure	0.1 MPa
Temperature	30, 60°C
Solution	0 and 1 wt% NaCl
Flow condition	Agitated, 200 rpm, 12.7 mm stir bar
Material	X65 with pyrrhotite layer
Corrosion measurement methods	LPR, EIS, and weight loss
pH <sub>2</sub> S in the gas phase	0, 0.01 MPa in N <sub>2</sub> or CO <sub>2</sub>
H <sub>2</sub> S concentration in the liquid phase	9.3 × 10 <sup>-3</sup> mol/L at 30°C 5.5 × 10 <sup>-3</sup> mol/L at 60°C
pH	4.0, 6.2 (±0.1)

were conducted with a three-electrode setup, where a pretreated disc electrode made of X65 pipeline steel with a pyrrhotite layer served as the working electrode (WE). A 20 mm × 30 mm platinum mesh was used as counter electrode (CE). A saturated silver/silver chloride (Ag/AgCl) reference electrode (RE) was connected via a salt bridge with a Luggin capillary. In addition to the steel WE, four small square steel specimens with a surface area of 3.4 cm<sup>2</sup> were included in the cell for the purpose of surface analysis. The H<sub>2</sub>S gas concentration was maintained using gas rotameters and the accuracy of the concentration was confirmed by using a gas sample pump with colorimetric H<sub>2</sub>S detector tubes. The gas outlet was scrubbed using a 5 M sodium hydroxide solution (NaOH) and several dry carbon scrubbers to capture the H<sub>2</sub>S.

Prior to each experiment, the electrolyte was deoxygenated by sparging with either N<sub>2</sub> or CO<sub>2</sub> gas for at least 3 h prior to the addition of H<sub>2</sub>S gas. The H<sub>2</sub>S was introduced into the experimental cell at the desired concentration for at least 1 h prior to immersion of the specimens, in order to ensure that the electrolyte was in equilibrium with respect to aqueous H<sub>2</sub>S. The electrolyte was stirred at 200 rpm with a 12.7 mm stir bar to ensure proper mixing. The solution pH was adjusted to the desired value by adding a deoxygenated 1 M hydrochloric acid (HCl) or NaOH solution. Then, the X65 specimens were inserted into the glass cell.

The corrosion processes were monitored via OCP, linear polarization resistance (LPR), and electrochemical impedance spectroscopy (EIS) measurements. The measured polarization resistance ( $R_p$ ) obtained from LPR was corrected for ohmic drop using the solution resistance ( $R_s$ ) measured by EIS. The Tafel slopes used to calculate the corrosion rate from the  $R_p$  values were: -0.12 V/decade for the cathodic reaction and 0.04 V/decade for the anodic reaction. Similar Tafel slopes were reported by Zheng, et al.,<sup>3-5</sup> and Esmacely, et al.,<sup>47</sup> in the presence of H<sub>2</sub>S across different experimental conditions at different pH. The abovementioned authors have explicitly identified that the Tafel

slope for direct reduction of H<sub>2</sub>S was also approximately -0.12 V/decade.

### *Specimen Pretreatment (Pyrrhotite Layer Generation)*

In order to study the effect of the pyrrhotite layer on localized corrosion, the X65 steel specimens were “pretreated” in a different experimental setup, used to develop a reproducible pyrrhotite layer prior to their immersion into the electrochemical glass cell described above.<sup>48-49</sup>

In high-temperature sulfidation of steel in crude oil fractions seen in refinery conditions, pyrrhotite is most often found as a corrosion product. Such pyrrhotite is the same compound as seen in aqueous corrosion of steel in the presence of H<sub>2</sub>S. This was used, following the procedure described below, to reproducibly form a pyrrhotite layer on steel that could be used in subsequent experimentation. The thickness of the pyrrhotite layer was controlled by the duration of the high-temperature sulfidation experiment. Its purity was established by utilizing x-ray diffraction (XRD) analysis. The structure and properties of the high-temperature pyrrhotite layer were assumed to be the same as what is formed in aqueous H<sub>2</sub>S environments.

Specimen pretreatment, which was used to form a pyrrhotite layer on the steel surface, was performed in a 1 L Inconel<sup>†</sup> autoclave. A mineral oil with a sulfur content of 0.25 wt% was used to form the pyrrhotite layer on the steel surfaces. The autoclave had a magnetic stirrer that drives an internal impeller that homogenizes the pretreatment fluid and ensures good heat transfer. Two types of specimens made of X65 steel were pretreated in the 1 L autoclave. The first type were small square specimens with a surface area of 3.4 cm<sup>2</sup> and the second type were large cylindrical specimens with the active surface being 7.9 cm<sup>2</sup>. The small square specimens were suspended using Inconel<sup>†</sup> wires and completely submerged in the experimental fluid during the pretreatment. The large cylindrical specimens were placed on the bottom of the autoclave with the flat corroding surface facing upward.

At the beginning of the pretreatment procedure, nitrogen gas was used to purge and pressurize the autoclave headspace to 1.5 MPa, when the heating was turned on. The autoclave reached the preset temperature of 343°C after approximately 1.5 h and then maintained for 24 h under continuous stirring. At the end of the pretreatment procedure, the heating and stirring were turned off and the autoclave was allowed to gradually cool down to room temperature. Before opening the autoclave, the headspace was purged with N<sub>2</sub> to remove any gases generated during the pretreatment procedures. The specimens were extracted from the oil and stored in a chemically inert mineral oil until further use in corrosion experiments. Prior to each corrosion experiment, the pretreated specimens

<sup>†</sup> Trade name.

were thoroughly rinsed with toluene and acetone to remove all oil residues from their surfaces and washed with isopropanol.

### Pyrrhotite Layer Surface Analysis

The morphology of the corrosion product layer was analyzed utilizing a scanning electron microscope (SEM, JEOL 6390LV<sup>†</sup>). Compositional analyses were performed using a Rigaku Ultima IV<sup>†</sup> x-ray diffractometer with Cu K $\alpha$  radiation from 10 to 70 2 $\theta$ . An Alicona Infinite Focus G4<sup>†</sup> profilometer was used to measure pit depth.

## RESULTS AND DISCUSSION

A detailed discussion of the experimental results will follow the review of characterization data for the pretreated specimens.

### Pretreated Specimens

Figure 1 shows the SEM image of the corroded (top) surface and cross-section image of the pretreated specimens. In Figure 1(a), one can see that there are two layers, a loose layer on top of a more compact layer underneath, and each has a similar gross morphology; the visual difference between the upper and lower layer is associated with delamination phenomena routinely observed for iron sulfides grown on steel. The cross-section image in Figure 1(b) demonstrates that the layer on the pretreated specimen is continuous and is well attached to the surface.

Figure 2 shows the XRD pattern of the pretreated specimen. Based on initial peak analysis,<sup>50</sup> troilite seemed to be the main component of the layer; however, a more thorough analysis revealed otherwise as described below.

Implementing a procedure as suggested by Arnold and Reichen,<sup>51</sup> who reported a relationship between the d-spacing corresponding to the (102) plane for pyrrhotite and the atomic percentage of metallic components, the Fe<sup>2+</sup> content in the pretreated layer was determined. The authors<sup>51</sup> generated a graph for

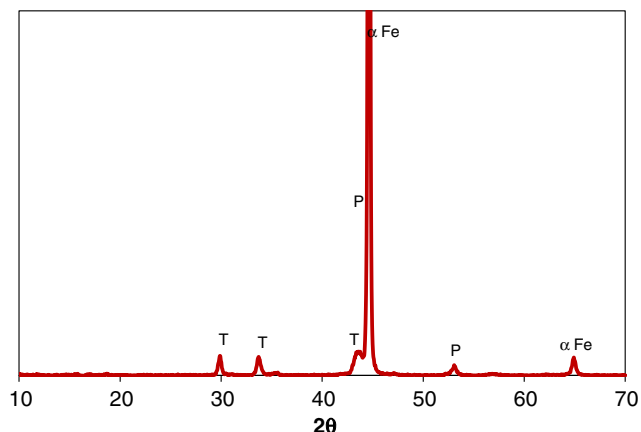


FIGURE 2. XRD pattern of the pretreated X65 specimens. P: pyrrhotite, T: troilite.

(102) d-spacing values versus iron content in at% for pyrrhotite. Utilizing this graph, the Fe<sup>2+</sup> content of generated pyrrhotite layers was obtained. The obtained Fe<sup>2+</sup> and the thermodynamic plot of temperature vs. phase formation of iron sulfides reported by Desborough and Carpenter<sup>52</sup> was used to characterize the composition of the layer. It was concluded that the layer was mostly composed of pyrrhotite with some troilite. This was later confirmed by using XRD quantitative analysis (using the PDXL<sup>†</sup> software).

### Part 1: Corrosion of Steel with a Preformed Pyrrhotite Layer Exposed to an Aqueous CO<sub>2</sub> Solution

In aqueous CO<sub>2</sub> corrosion, the pretreated specimen with a pyrrhotite layer was studied under two conditions: in a conductive 1 wt% NaCl electrolyte and a poorly conductive DI water in order to investigate the role of galvanic coupling. However, LPR measurements were not conducted in the experiments without NaCl because of the low solution conductivity. The solution pH, which was monitored for the duration of the experiments, was relatively stable (changing from pH 4.0 to pH 4.5).

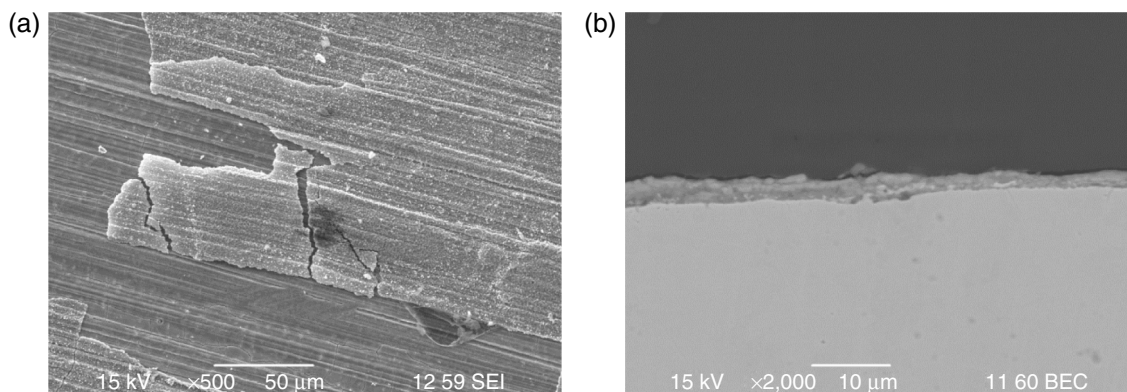
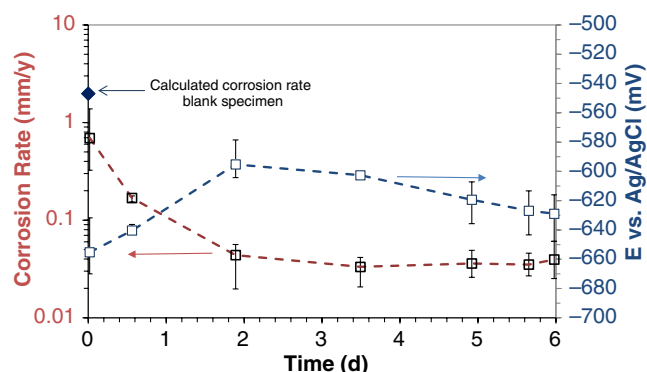


FIGURE 1. SEM images of representative pretreated steel specimen. (a) Top surface, and (b) cross section.



**FIGURE 3.** Corrosion rate of X65 specimen with pyrrhotite-type layer vs. time of a sparged solution with 0.097 MPa CO<sub>2</sub> at 30°C and pH 4.0.

Figure 3 shows the average corrosion rate of the pretreated specimen exposed to a CO<sub>2</sub> saturated solution with 1 wt% NaCl. This experiment was repeated four times. The average of the measured data is reported with the error bars denoting the maximum and minimum values. The initial corrosion rate was approximately 0.7 mm/y, compared to the expected bare steel corrosion rate of about 2.0 mm/y (as calculated using the mechanistic corrosion model described by Zheng, et al.<sup>4</sup>). The comparison indicates that the preformed pyrrhotite layer did offer some protection to the steel surface underneath. However, the initial corrosion rate was not as low as one would expect as a result of a compact and protective layer. When the corrosion rate is controlled by the rate of cathodic reduction then the conductive nature of the pyrrhotite layer should increase the uniform corrosion rate; this can be offset by the same porous layer acting as a diffusion barrier, which should have decreased the corrosion rate. Either way, over a period of 3 d the corrosion rate decreased to less than 0.1 mm/y. The specimen OCP increased approximately 20 mV during the experiment.

Figure 4 shows the SEM image of the pretreated specimens after exposure to the aqueous CO<sub>2</sub> solutions.

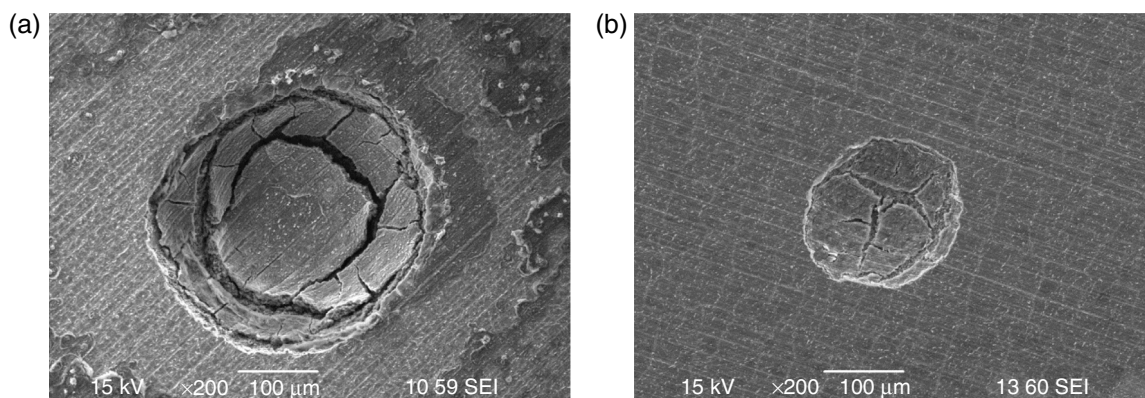
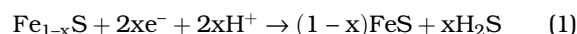


**FIGURE 4.** SEM image of pretreated specimen after exposure to an aqueous solution sparged with 0.097 MPa CO<sub>2</sub> at 30°C and pH 4.0. (a) 1 wt% NaCl, and (b) no NaCl.

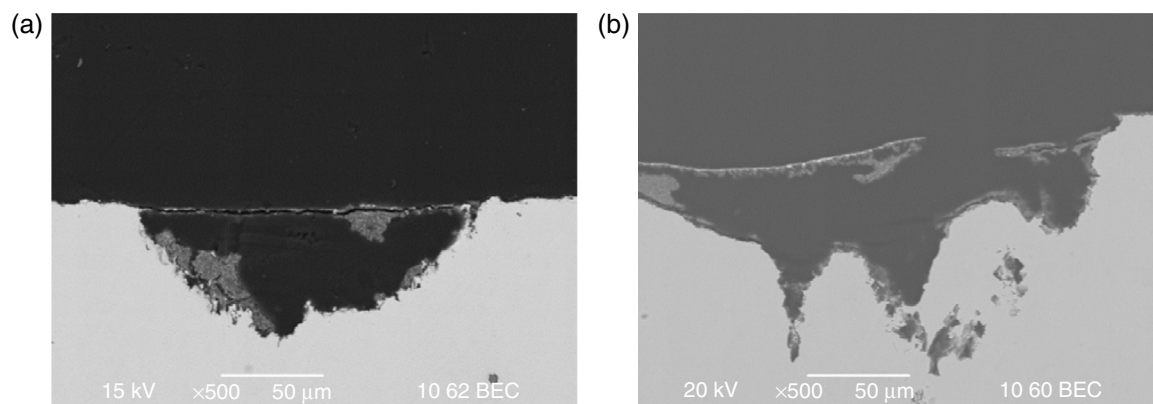
Irrespective of the presence of NaCl, the top layers on both images (Figures 4[a] and [b]) appeared to be similar—with locations where the layer locally collapsed, which were later identified to be points of localized corrosion. Overall, the top layer morphology changed as a result of exposure to the aqueous CO<sub>2</sub> solution as compared to the original surface shown in Figure 1(a).

Figure 5 shows cross sections of pits formed on the pretreated specimens exposed to the aqueous CO<sub>2</sub> solution with and without NaCl. Small amount of corrosion product was found in the pits, which suggests they were still actively corroding at the time when specimens were retrieved. The area in the vicinity of the pits on both images show that the corrosion product layer was thin, therefore undetectable with XRD.

Experimental observation of the pretreated specimens revealed that the preformed pyrrhotite layer underwent dissolution upon its exposure to the aqueous CO<sub>2</sub> solution. Because the preformed layer was not in a thermodynamically stable condition, dissolution of the layer was expected under these test conditions. There have been multiple mechanisms proposed for pyrrhotite dissolution in acidic media.<sup>53-56</sup> One of the reductive mechanisms suggests that H<sup>+</sup> adsorbs onto “anionic sites” on the surface of the pyrrhotite crystals, and this results in a transformation from a nonstoichiometric pyrrhotite to stoichiometric troilite (Reaction [1]) with production of H<sub>2</sub>S. This is followed by dissolution of troilite to form HS<sup>-</sup> and Fe<sup>2+</sup> shown by Reaction (2).<sup>53-55,57-60</sup>



In the current study, it seems that the preformed pyrrhotite layer underwent a dissolution process, which initially started locally and then proceeded to dissolve completely over time. Localized corrosion initiated on these local sites, where the preformed layer dissolved first, leaving a galvanic cell between the exposed steel surface and the remaining pyrrhotite layer. The iron



**FIGURE 5.** Cross-section image of pretreated specimen after exposure to an aqueous solution sparged with 0.097 MPa  $\text{CO}_2$  at 30°C and pH 4.0. (a) 1 wt% NaCl, and (b) no NaCl.

dissolution at the anode is accelerated by an additional cathodic reaction on the surrounding semiconductive pyrrhotite layer.

Pyrrhotite is a semiconductive iron sulfide, which in a conductive solution forms a galvanic cell when in direct contact with a steel surface. Table 1 shows that pyrrhotite's potential is more positive compared to the steel surface.<sup>39-41</sup> Therefore, the steel surface becomes the anode and corrodes at a higher rate. This galvanic attack is accelerated because of a high cathode/anode surface area ratio, caused by the porous nature of the pyrrhotite layer, which is expected to enhance the rate of  $\text{H}^+$  reduction.<sup>42</sup>

Figure 6 shows the XRD patterns of the pretreated specimen surface before and after it was exposed for 6 d to the aqueous  $\text{CO}_2$  solution. The diffraction patterns indicate that the layer post-exposure was too thin to be detectable by conventional XRD, therefore confirming that the pyrrhotite layer dissolved by the end of the experiment.

There seems to be an additional process that took place at the same time. Dissolution of the pyrrhotite

layer produced small amounts of  $\text{H}_2\text{S}$  as described above (Reaction [1]), which then reacted with the adjacent steel surface, forming most likely a very thin mackinawite layer. Utilizing XPS analysis, it was shown by Lee<sup>61</sup> that a thin mackinawite layer forms on the surface of a mild steel upon exposure to low concentrations of  $\text{H}_2\text{S}$ , even if it is undetectable by SEM/energy-dispersive x-ray spectroscopy (EDS)/XRD. This mackinawite layer probably led to a reduction of the uniform corrosion rate, as shown in Figure 3(a), but did not affect the localized corrosion.

To confirm the galvanic nature of the observed localized attack, the conductivity of the aqueous solution was varied, which was expected to have a pronounced effect on the magnitude of the galvanic current. To that effect, experiments were conducted in the presence and absence of NaCl. Before the results are presented, it should be noted that in the literature, the role of chloride in localized corrosion is contradictory.<sup>22,28,62-65</sup> While some researchers have attributed localized corrosion initiation of mild steel to the presence of chlorides, work by Fang<sup>22</sup> revealed that the dominant effect is via solution conductivity. Thus, the role of NaCl on localized corrosion in the present study is attributed primarily to its impact on solution conductivity.

Figure 7 shows the SEM images of the pretreated specimens after exposure to solutions with and without NaCl and after the corrosion product layer was chemically removed using Clarke's solution following the procedure described in ASTM Standard G1.<sup>66</sup> Localized corrosion was observed on both specimens. Profilometry was utilized to measure the depth of the pits and to calculate the time averaged pit penetration rate:  $\text{PPR} = h/t$ , where  $h$  is the deepest pit depth in mm, and  $t$  is the time in years. Figure 8 shows the profilometry images, indicating that the specimen exposed to a more conductive solution was attacked at a much higher rate (13.7 mm/y) than the specimen exposed to the less conductive solution (4.2 mm/y). Uniform bare steel corrosion rate under these

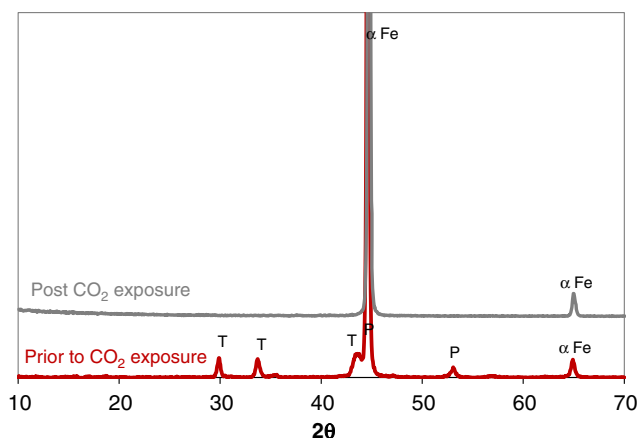


**FIGURE 6.** XRD of the pretreated specimen after exposure to an aqueous solution sparged with 0.097 MPa  $\text{CO}_2$  at 30°C and pH 4.0. P: pyrrhotite, T: troilite.

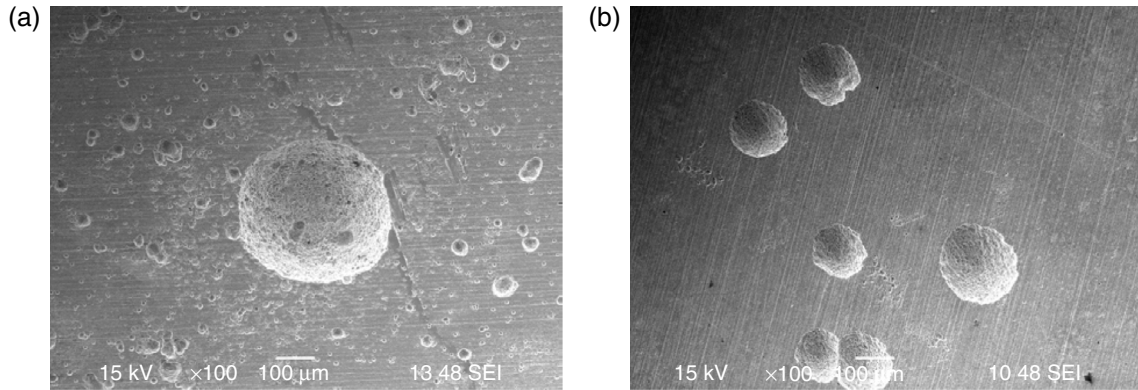


**FIGURE 7.** SEM image of pretreated specimen after exposure to an aqueous solution sparged with 0.097 MPa CO<sub>2</sub> at 30°C and pH 4.0 without corrosion product layer. (a) 1 wt% NaCl, and (b) no NaCl.

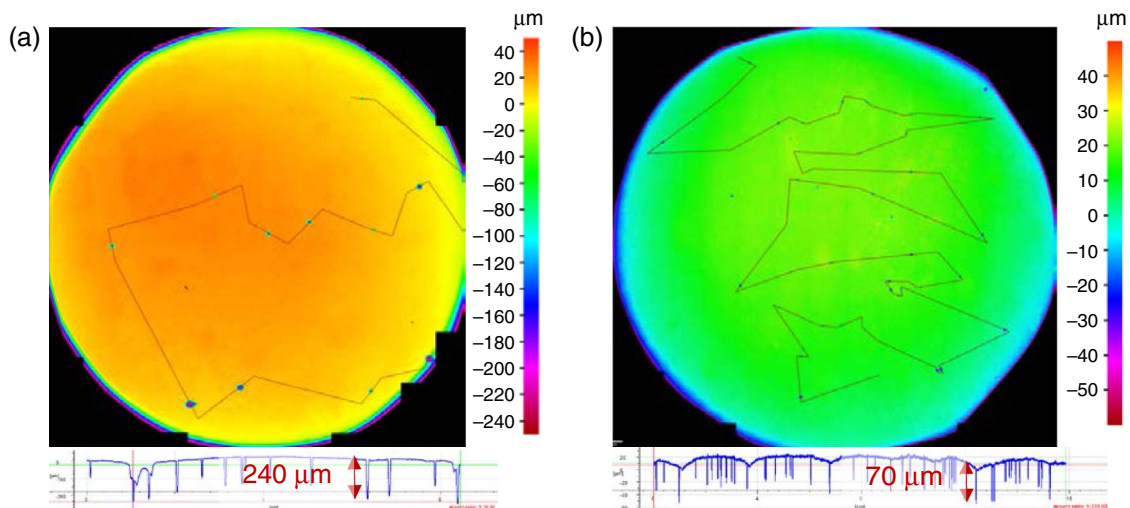


**FIGURE 8.** Profilometry image of pretreated specimens after exposure to an aqueous solution sparged with 0.097 MPa CO<sub>2</sub> at 30°C and pH 4.0 without layer. (a) 1 wt% NaCl, and (b) no NaCl.

conditions is of the order of 2 mm/y to 3 mm/y making the localized attack in the conductive solution particularly severe, confirming its galvanic nature (see Figure 9).

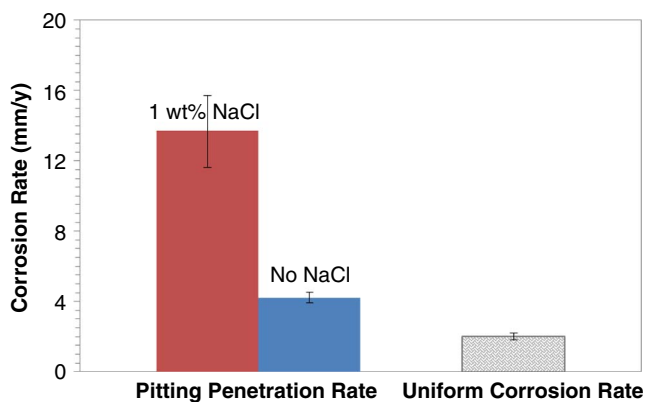


**FIGURE 9.** Pit penetration rate of the specimens in an aqueous solution sparged with 0.097 MPa CO<sub>2</sub> at 30°C and pH 4.0.

### Part 2: Corrosion of Steel with a Preformed Pyrrhotite Layer Exposed to Aqueous H<sub>2</sub>S Solution

Figure 10 shows the average LPR corrosion rate and the OCP data (from two repeated experiments) conducted with the pretreated specimen exposed to an aqueous solution sparged with 0.01 MPa H<sub>2</sub>S at two different conditions. The conditions were selected based on the thermodynamic stability of the pyrrhotite layer. In the first condition, the pyrrhotite layer should have been thermodynamically stable (the solution was slightly supersaturated) and was not expected to dissolve (60°C and pH 6.2±0.1). The second condition (30°C and pH 4.0±0.1) was selected so that pyrrhotite was not thermodynamically stable (the solution was under-saturated), and it was expected to dissolve. Experiments for each of these two conditions were repeated.

The initial corrosion rate was rather high and similar to that obtained with a bare steel (blank) under

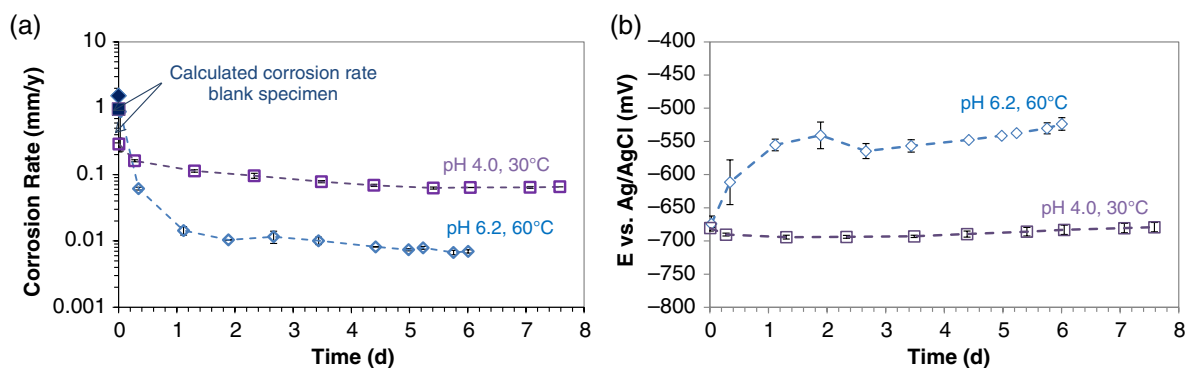


**FIGURE 10.** (a) Corrosion rate of pretreated specimen. (b) The OCP vs. time in an aqueous solution sparged with 0.01 MPa  $H_2S$  in  $N_2$ , 1 wt% NaCl.

the same conditions (as calculated by the mechanistic model described by Zheng, et al.<sup>2-4</sup>), suggesting that the preformed pyrrhotite layer did not initially offer any appreciable corrosion protection to the steel surface in these conditions. However, the corrosion rate decreased significantly within the first day of exposure to a value close or less than 0.1 mm/y depending on the experimental conditions (Figure 10[a]). The OCP change over time (Figure 10[b]) shows a stable OCP throughout the experiment for the pH 4.0 and 30°C condition, while for the experiment at pH 6.2 and 60°C, OCP increased approximately by 100 mV.

The bulk pH did not change significantly for the case where the pyrrhotite layer was thermodynamically stable and did not dissolve (at pH 6.2). However, when the pyrrhotite layer dissolved, the bulk pH increased from initial pH 4.0 to pH 5.0, bringing it close to saturation for pyrrhotite.

Figure 11 shows the SEM images of the specimen at the end of the experiment. It can be observed that the pretreated specimen exposed to the thermodynamically stable condition was uniformly covered by a corrosion product layer, Figure 11(a). However, the specimen initially exposed to the under-saturated solution, Figure 11(b), shows evidence of damage to the

initial corrosion product layer as well as a layer below and some precipitation on top. Cross-section analyses were performed to identify the thickness and the morphology of these layers. Figure 12 shows that in both experimental conditions there was a bilayer on the surface. For the specimen exposed to the thermodynamically stable condition, Figure 12(a), the original pyrrhotite layer seems to be intact (having a similar thickness as that shown in Figure 1[b]), with an additional layer on top. For the specimen exposed to the under-saturated solution, the final corrosion product layer is much thinner because of pyrrhotite dissolution, Figure 12(b).

XRD analysis was conducted on specimens after their exposure to the aqueous  $H_2S$  solution, in order to characterize the layers and any possible compositional change. Figure 13 shows the XRD patterns of the pretreated specimens before and after exposure to the two experimental conditions. The extra peaks seen on the two exposed specimens were identified to be mackinawite, marked as "M," and troilite, marked as "T." The appearance of troilite was expected because the product of a non-stoichiometric pyrrhotite transformation is a stoichiometric troilite (Reaction [1]).<sup>54,57-58</sup> Mackinawite has a similar

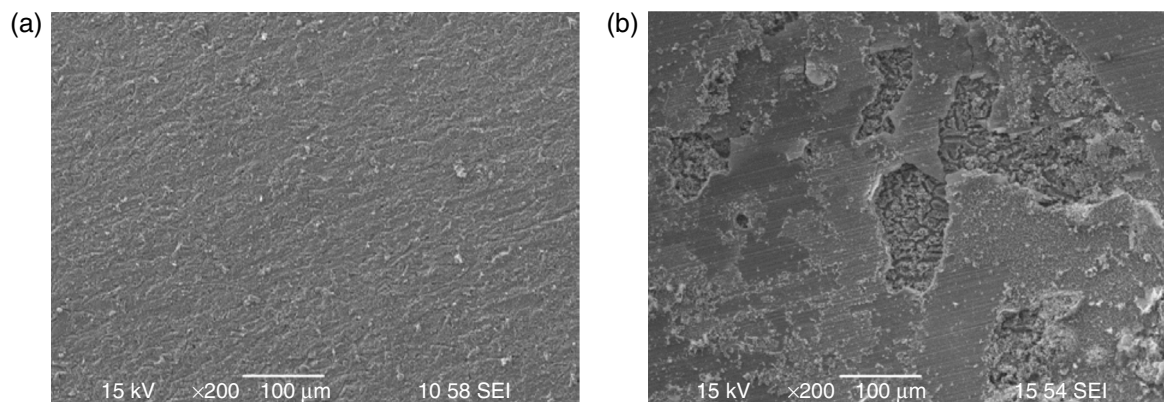


**FIGURE 11.** SEM image of pretreated specimen after exposure to an aqueous solution sparged with 0.01 MPa  $H_2S$ , 1 wt% NaCl at: (a) 60°C and pH 6.2, and (b) 30°C and pH 4.1.

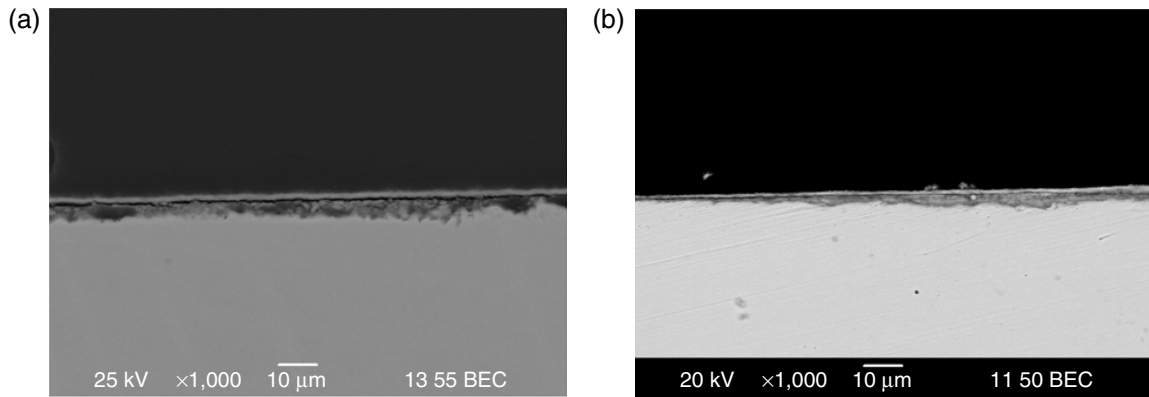


**FIGURE 12.** Cross-section image of pretreated specimen after exposure to an aqueous solution sparged with 0.01 MPa  $H_2S$ , 1 wt% NaCl at: (a) 60°C and pH 6.2, and (b) 30°C and pH 4.1.

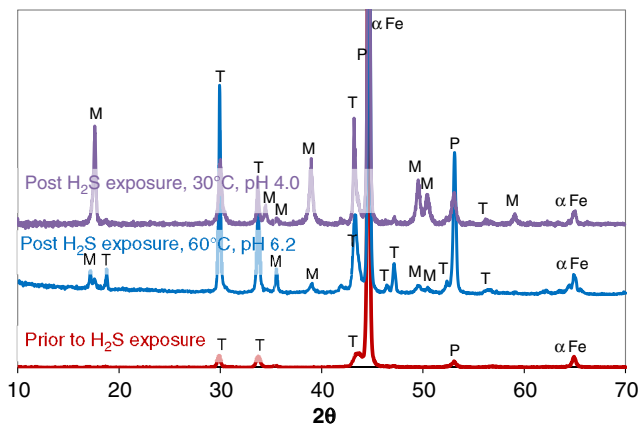


**FIGURE 13.** XRD of the pretreated specimen after exposure to an aqueous solution sparged with 0.01 MPa  $H_2S$  at 60°C and pH 6.2, and at 30°C and pH 4.0, 1 wt% NaCl. P: pyrrhotite, T: troilite, M: mackinawite.

solubility as pyrrhotite and appears to have precipitated. One could wonder why pyrite was not observed on the XRD analysis post  $H_2S$  exposure. Less stable iron sulfides usually transform to the more stable iron

sulfide polymorphs after longer exposures depending on thermodynamic conditions. In order to form pyrite, much higher pH, higher potentials, or higher temperatures are required. The experiments described in the current manuscript were conducted at conditions where pyrite was not thermodynamically stable. Thus, it was not expected to observe any pyrite on the specimens. It is noteworthy that pyrite has a slow kinetics of formation which makes it even more difficult to obtain in laboratory experimentation.

Figure 14 shows the SEM image of the specimens after the corrosion product layer was removed using Clarke's solution.<sup>66</sup> Figure 14(a) shows a uniformly corroded surface of the specimen exposed to a thermodynamically stable condition, while Figure 14(b) shows a non-uniform attack of the steel surface of the specimen exposed to the under-saturated solution. However, this non-uniform attack could not be detected in the profilometry image of the same surface shown in Figure 15, which indicates that these areas were rather shallow. In summary, no galvanic localized attack was detected in these experiments, at least not in the same way as was seen in  $CO_2$  experiments reported above.

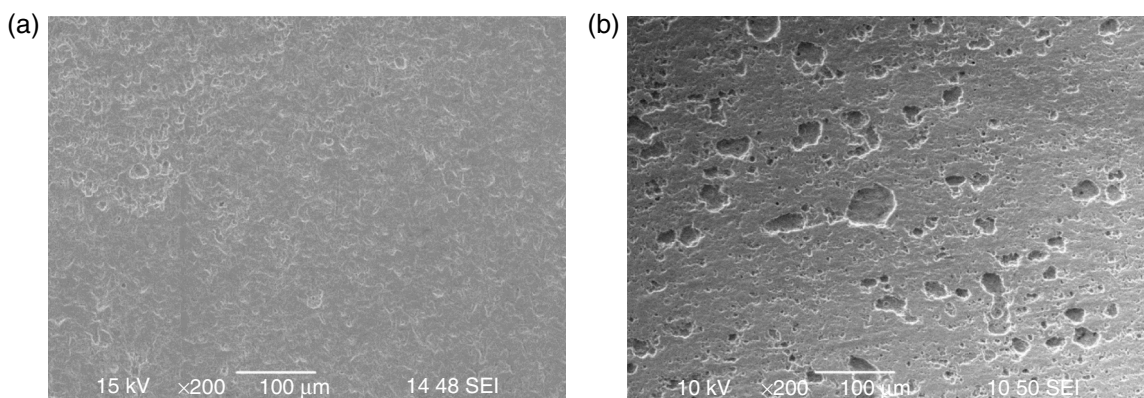


**FIGURE 14.** SEM image of the pretreated specimen after exposure to an aqueous solution sparged with 0.01 MPa  $H_2S$ , 1 wt% NaCl at: (a) 60°C and pH 6.2, and (b) 30°C and pH 4.0, after removal of the corrosion product layer.

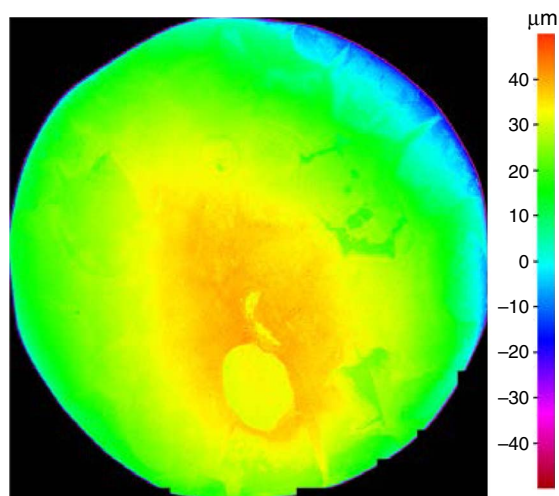


**FIGURE 15.** Profilometry image of the pretreated specimen after exposure to an aqueous solution sparged with 0.01 MPa H<sub>2</sub>S, 1 wt% NaCl at 30°C and pH 4.0 without layer.

The cross-section images in Figure 12 show that upon exposure to the aqueous H<sub>2</sub>S solution, the preformed pyrrhotite layer was covered with a dense top layer where the pores were most likely filled with the secondary corrosion product layer. Based on XRD analyses, it is most likely that this layer was composed of precipitated mackinawite and possibly troilite/pyrrhotite. It is here hypothesized that this layer, once it formed, has “blocked” the preformed pyrrhotite layer and the steel surface underneath, by limiting the mass transfer of species. Thus, any galvanic cell between the steel surface and the pyrrhotite layer was disrupted and, as a result, localized corrosion was retarded. In the experiment conducted in a supersaturated solution, the dense top layer precipitated fast and therefore no localized attack is seen in Figure 14(a). For the initially under-saturated solution, the dense top layer formed after approximately 2 d when the bulk solution reached saturation; in the interim the pyrrhotite layer partially dissolved and localized attack was initiated, which was then arrested as a result of the formation of the

dense top layer. This is evidenced by the shallow pits seen in Figure 14(b).

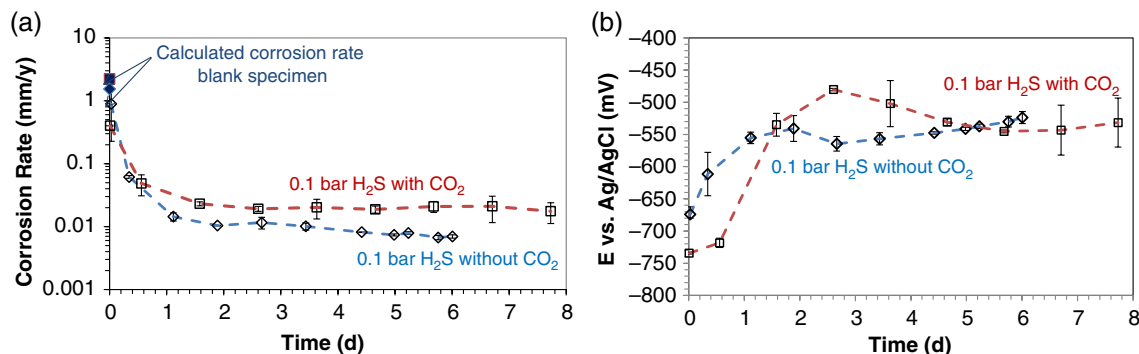
### Part 3: Corrosion of Steel with a Preformed Pyrrhotite Layer Exposed to a Mixed CO<sub>2</sub>/H<sub>2</sub>S Solution

In Part 1 of the present study, it was shown that localized corrosion was observed on pretreated specimens exposed to an aqueous CO<sub>2</sub> solution, because of the uneven dissolution of the pyrrhotite layer which led to galvanic corrosion. In Part 2, it was shown that in an aqueous H<sub>2</sub>S solution, localized corrosion did not take place as a result of a dense layer formation on top of the pyrrhotite layer. It is therefore of interest to investigate the possibility of localized corrosion in mixed CO<sub>2</sub>/H<sub>2</sub>S environments, which corresponds to more realistic conditions encountered in the field.

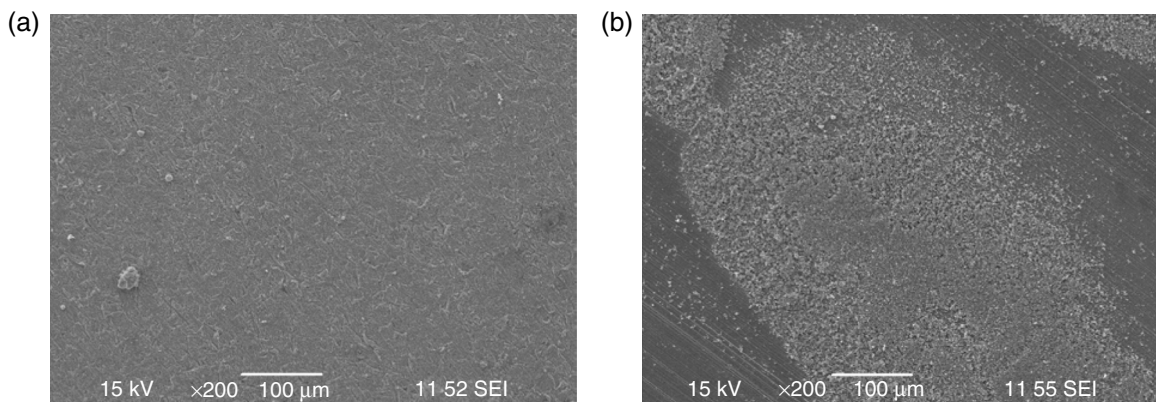
As shown in Figure 16(a), the uniform corrosion rate was higher with CO<sub>2</sub> present than without it for the same partial pressure of H<sub>2</sub>S. The calculated<sup>3-5</sup> bare steel corrosion rate is also shown in Figure 16(a). The pH in the bulk solution was reasonably stable ( $\pm 0.1$  pH unit) throughout the experiments with and without CO<sub>2</sub>. The OCP change of the pretreated specimens exposed to the experimental condition in Figure 16(b) shows approximately 100 mV to 200 mV potential change for the specimen upon their exposure to the experimental solution.

Figure 17(a) shows the SEM images of the top surface the specimen after the exposure to an H<sub>2</sub>S-only solution (in the absence of CO<sub>2</sub>), where a uniform corrosion product can be seen. A non-uniform appearance of the corrosion product layer is found in the presence of CO<sub>2</sub>, Figure 17(b). If one compares the image in Figure 1(a) of the pyrrhotite layer before exposure and the image in Figure 17(b) after exposure to the mixed CO<sub>2</sub>/H<sub>2</sub>S environment, one can observe the partial transformation of the original pyrrhotite layer.

This is confirmed in Figure 18(b), where the thinning of the original pyrrhotite layer is obvious. According to the cross-section image of the pretreated specimen in Figure 1(b), the preformed pyrrhotite layer



**FIGURE 16.** (a) Corrosion rate. (b) OCP of pretreated specimen vs. time sparged with 0.01 MPa H<sub>2</sub>S with and without 0.07 MPa CO<sub>2</sub>, at pH 6.1 and 60°C, 1 wt% NaCl.



**FIGURE 17.** SEM image of pretreated specimen after exposure to an aqueous solution sparged with 0.01 MPa  $H_2S$ , 1 wt% NaCl at 60°C and pH 6.2. (a) No  $CO_2$ , and (b) 0.07 MPa  $CO_2$ .

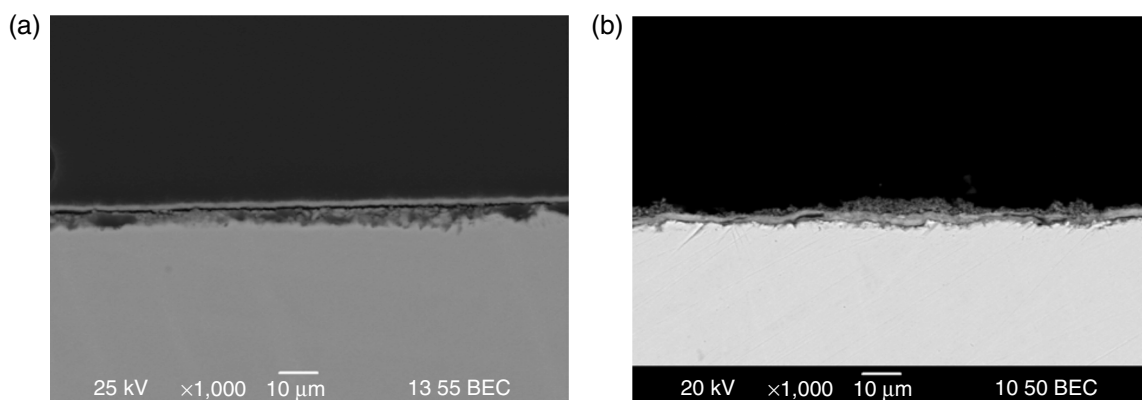


**FIGURE 18.** Cross-section image of pretreated specimens after exposure to an aqueous solution sparged with 0.01 MPa  $H_2S$ , 1 wt% NaCl at 60°C and pH 6.2. (a) No  $CO_2$ , and (b) 0.07 MPa  $CO_2$ .

was approximately 3  $\mu m$  to 4  $\mu m$ . After exposure to 0.1 bar (0.01 MPa)  $H_2S$  in the absence of  $CO_2$  as shown in Figure 18(a), the layer grew to approximately 5  $\mu m$  to 6  $\mu m$ , while it thinned to around 2  $\mu m$  when exposed to 0.1 bar  $H_2S$  and 0.7 bar (0.07 MPa)  $CO_2$ , Figure 18(b). In the absence of  $CO_2$ , there is a dense top layer that formed as shown in Figure 18(a) and also in Figure 12(a) for a different location. However, this type of layer has not formed in the presence of  $CO_2$  and an appearance of a different “fluffy” phase can be seen. Also, the pyrrhotite layer seems to have been locally detached from the steel surface in the presence of  $CO_2$ , which was not the case in the  $H_2S$ -only environment.

XRD analyses were performed to determine the composition of the layer on the specimens as the pre-formed pyrrhotite underwent some transformation in the presence of  $CO_2$ . The intensity of the peaks associated with troilite/mackinawite is stronger for the specimen exposed to the  $H_2S$ -only solution (see Figure 19). It is believed that the “fluffy” phase seen in Figures 17(b) and 18(b) is mackinawite.

Following removal of the layer, Figure 20(b) shows that the steel surface exposed to the mixed

$CO_2/H_2S$  solution underwent localized corrosion, which was not the case in the absence of  $CO_2$ , see Figure 20(a). This could be explained by the fact that a different layer formed on the specimens upon exposure

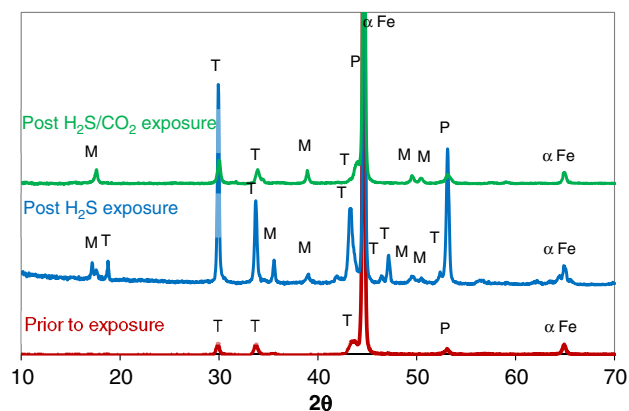


**FIGURE 19.** XRD of the pretreated specimens after exposure to an aqueous solution sparged with 0.01 MPa  $H_2S$  at 60°C and pH 6.2 with and without 0.07 MPa  $CO_2$ , 1 wt% NaCl. P: pyrrhotite, T: troilite, M: mackinawite.

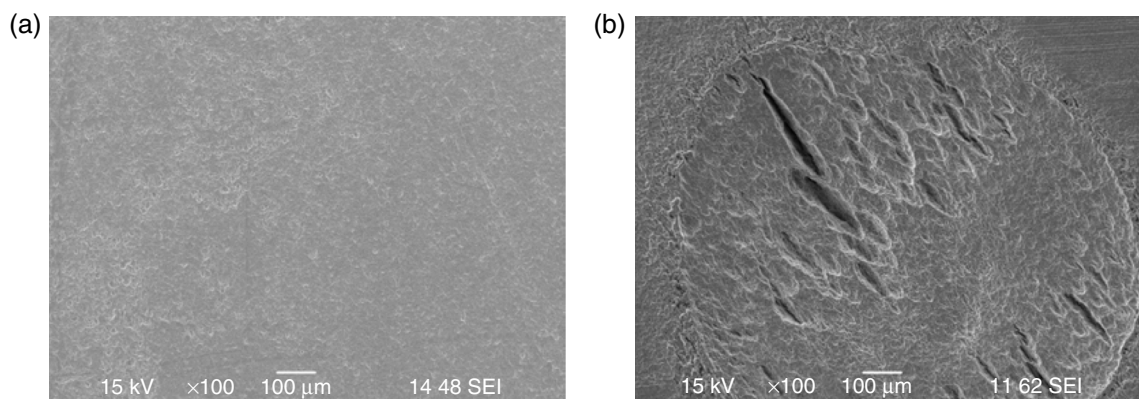


**FIGURE 20.** SEM image of the pretreated specimens after exposure to an aqueous solution sparged with 0.01 MPa H<sub>2</sub>S, 1 wt% NaCl at 60°C and pH 6.2: (a) without CO<sub>2</sub>, and (b) 0.07 MPa CO<sub>2</sub>, after removal of the corrosion product layer.

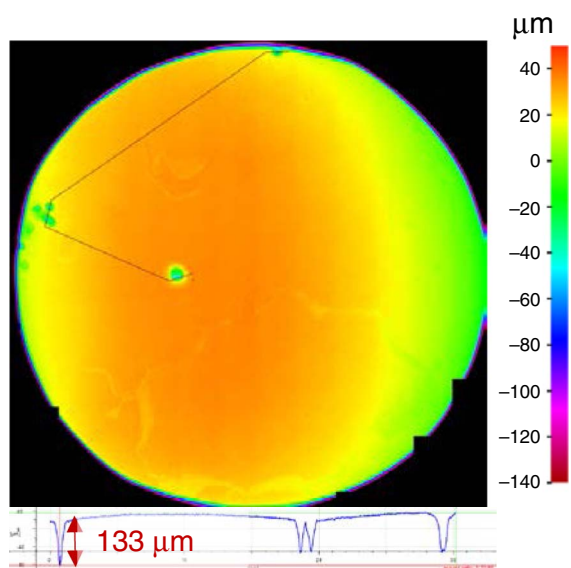


**FIGURE 21.** Profilometry image of pretreated specimen after exposure to an aqueous solution sparged with 0.01 MPa H<sub>2</sub>S, 0.07 MPa CO<sub>2</sub>, 1 wt% NaCl at 60°C and pH 6.2 without layer.

to different experimental conditions: a dense more protective layer formed in the H<sub>2</sub>S-only solution and a “fluffy” mackinawite layer formed in the mixed CO<sub>2</sub>/H<sub>2</sub>S solution.

Profilometry was utilized to measure the depth of the observed pits. Figure 21 shows that the localized attack was found only in one section on the steel surface with the maximum pit depth of 133 μm corresponding to 5.5±0.5 mm/y pit penetration rate. It should be noted that these experiments were repeated. In both experiments there were only a few pits concentrated in a limited area.

## CONCLUSIONS

❖ Localized corrosion occurred in an aqueous CO<sub>2</sub> solution with and without NaCl, where the conductive pyrrhotite layer underwent non-uniform dissolution,

resulting in partial exposure of the steel surface, forming a galvanic couple.

❖ In an aqueous CO<sub>2</sub> solution, the presence of 1 wt% NaCl led to a higher solution conductivity, where the localized corrosion rates were found to be approximately three times higher than the localized corrosion rate in the absence of NaCl, which confirmed the galvanic nature of the attack.

❖ Localized corrosion was found to a lesser extent in a mixed CO<sub>2</sub>/H<sub>2</sub>S aqueous solution containing 1 wt% NaCl, where the local dissolution of the pyrrhotite layer was slower and a partially protective mackinawite layer formed.

❖ A dense protective layer formed on top of the pyrrhotite layer on the specimen exposed to an aqueous H<sub>2</sub>S solution with 1 wt% NaCl. Thus, the preformed pyrrhotite layer dissolution was slowed down significantly, and no localized attack was observed.

❖ Overall, it is concluded that when a non-uniform semiconductive pyrrhotite layer is in contact with the steel surface in a corrosive electrolyte, this could lead to galvanically-driven localized corrosion.

## ACKNOWLEDGMENTS

The authors acknowledge the financial support from a joint industry project including BP, Champion Technologies, Chevron, ConocoPhillips, DNV GL, ENI S.p.A., ExxonMobil, Hess, MultiChem, NALCO Energy Services, Occidental Petroleum Co., Petrobras, PETRONAS, PTT, Saudi Aramco, Inpex Corporation, SINOPEC, TOTAL, TransCanada, WGIM, and Shell. The authors would like to extend their appreciation to Dr. David Young and Dr. Bert Pots for their advice and contribution for the current study.

## REFERENCES

1. S. Nešić, “Carbon Dioxide Corrosion of Mild Steel,” in *Uhlig’s Corrosion Handbook*, ed. R. Winston Revie, 3rd ed. (Hoboken, NJ: John Wiley & Sons, Inc., 2011), p. 229-245.

2. W. Sun, S. Nešić, "Corrosion in Acid Gas Solutions," in *Shreir's Corrosion*, ed. J.A. Richardson, 2nd ed. (Oxford, United Kingdom: Elsevier, 2010), p. 1270-1298.
3. Y. Zheng, B. Brown, S. Nešić, *Corrosion* 70 (2014): p. 351-365.
4. Y. Zheng, J. Ning, B. Brown, S. Nešić, *Corrosion* 71 (2015): p. 316-325.
5. Y. Zheng, J. Ning, B. Brown, S. Nešić, *Corrosion* 72 (2016): p. 679-691.
6. F. Shi, L. Zhang, J. Yang, M. Lu, J. Ding, H. Li, *Corros. Eng. Sci. Technol.* 102 (2016): p. 1521-1557.
7. J. Ning, Y. Zheng, B. Brown, D. Young, S. Nešić, *Corrosion* 71 (2015): p. 945-960.
8. D.W. Shoesmith, P. Taylor, M.G. Bailey, D.G. Owens, *J. Electrochem. Soc.* 127 (1980): p. 1007-1015.
9. L.G. Benning, R.T. Wilkin, H. Barnes, *Chem. Geol.* 167 (2000): p. 25-51.
10. W.H. Thomason, "Formation Rates of Protective Iron Sulfide Films on Mild Steel in H<sub>2</sub>S-Saturated Brine as a Function of Temperature," CORROSION 1978, paper no. 41 (Houston, TX: NACE International, 1978).
11. F.H. Meyer, O.L. Riggs, R.L. McGlasson, J.D. Sudbury, *Corrosion* 14 (1958): p. 69-75.
12. W. Zhao, Y. Zou, K. Matsuda, Z. Zou, *Corros. Sci.* 102 (2016): p. 455-468.
13. D.F. Pridmore, R.T. Shuey, *Am. Mineral.* 61 (1976): p. 248-259.
14. C.I. Pearce, A.D. Patrick, D.J. Vaughan, *Rev. Mineral. Geochem.* 61 (2006): p. 127-180.
15. R. Schieck, A. Hartmann, S. Fiechter, R. Konenkamp, H. Wetzell, *J. Mater. Res.* 5 (1990): p. 1567-1572.
16. P.K. Abrattis, R.A.D. Patrick, D.J. Vaughan, *Int. J. Mine. Process* 74 (2004): p. 41-59.
17. D.J. Vaughan, J.R. Craig, *Mineral Chemistry of Metal Sulfides*, 1st ed. (New York, NY: Vail-Ballou, 1978), p. 17-117.
18. A.R. Lennie, K.E.R. England, D. Vaughan, *Am. Mineral.* 80 (1995): p. 960-967.
19. K.D. Kwon, K. Refson, S. Bone, R. Qiao, W.L. Yang, Z. Liu, G. Sposito, *Phys. Rev. B* 83 (2011): p. 064402-1 to 064402-7.
20. P.W. Bolmer, *Corrosion* 21 (1965): p. 69-75.
21. S.P. Ewing, *Corrosion* 11 (1955): p. 497-501.
22. H. Fang, "Investigation of Localized Corrosion of Carbon Steel in H<sub>2</sub>S Environments" (Ph.D. diss., Ohio University, 2012).
23. D.D. MacDonald, B. Roberts, J.B. Hyne, *Corros. Sci.* 18 (1978): p. 411-425.
24. G. Schmitt, *Corrosion* 47 (1999): p. 285-308.
25. N. Yaakob, "Top of the Line Corrosion in CO<sub>2</sub>/H<sub>2</sub>S Environments" (Ph.D. diss., Ohio University, 2015).
26. N. Yaakob, F. Farelis, M. Singer, S. Nešić, D. Young, "Localized Top of the Line Corrosion in Marginally Sour Environments," CORROSION 2016, paper no. 7695 (Houston, TX: NACE, 2016).
27. J. Ning, Y. Zheng, B. Brown, D. Young, S. Nešić, *Corrosion* 73 (2017): p. 155-168.
28. J. Kvarekvål, G. Svenningsen, "Effect of Iron Sulfide Deposits on Sour Corrosion of Carbon Steel," CORROSION 2016, paper no. 7313 (Houston, TX: NACE, 2016).
29. O. Yopez, N. Obeyesekere, J. Wylde, "Study of Sour Corrosion Mechanism Under Controlled pH," CORROSION 2016, paper no. 7795 (Houston, TX: NACE, 2016).
30. V. Brailovskiy, "Effect of Pre-Exposure of Sulfur and Iron Sulfide on H<sub>2</sub>S Corrosion at Different Temperatures" (Master's thesis, Universitetet i Stavanger, 2011).
31. R.C. Woollam, J.R. Vera, A. Huggins, W.H. Durine, "Localized Corrosion Due to Galvanic Coupling Between FeS-Covered and Uncovered Areas: Another Oilfield Myth?" CORROSION 2013, paper no. 2715 (Houston, TX: NACE, 2013).
32. J. Kvarekvål, "Corrosion Layer Breakdown and Localized Corrosion in CO<sub>2</sub>/H<sub>2</sub>S Environments," CORROSION 2012, paper no. 1537 (Houston, TX: NACE, 2012).
33. J. Kvarekvål, A. Dugstad, "Corrosion Mitigation with pH Stabilisation in Slightly Sour Gas/Condensate Pipelines," CORROSION 2006, paper no. 646 (Houston, TX: NACE, 2006).
34. K. Videm, J. Kvarekvål, *Corros. Sci.* 51 (1995): p. 260-269.
35. J. Kvarekvål, R. Nyborg, M. Seiersten, "Corrosion Product Films on Carbon Steel in Semi-Sour CO<sub>2</sub>/H<sub>2</sub>S Environments," CORROSION 2002, paper no. 296 (Houston, TX: NACE, 2002).
36. J. Kvarekvål, A. Dugstad, M. Seiersten, "Localized Corrosion on Carbon Steel in Sour Glycolic Solutions," CORROSION 2010, paper no. 277 (Houston, TX: NACE, 2010).
37. J. Kvarekvål, A. Dugstad, "Pitting Corrosion in CO<sub>2</sub>/H<sub>2</sub>S-Containing Glycol Solutions Under Flowing Conditions," CORROSION 2005, paper no. 631 (Houston, TX: NACE, 2005).
38. J. Amri, J. Kvarekvål, B. Malki, "Simulation of Solid-State Growth of Iron Sulfides in Sour Corrosion Conditions," CORROSION 2011, paper no. 078 (Houston, TX: NACE, 2011).
39. C. Almeida, B.F. Giannetti, *Electroanal. Chem.* 553 (2003): p. 27-34.
40. K.K. Mishro, K. Osseo-Asare, *Electrochem. Soc.* 135 (1988): p. 2502-2509.
41. L.C. Hamilton, R. Woods, *Electroanal. Chem.* 118 (1981): p. 327-343.
42. D.A. Jones, *Principles and Prevention of Corrosion*, 2nd ed. (Upper Saddle River, NJ: Prentice-Hall, 1996), p. 168-198.
43. K. Adam, K.A. Natarajan, S.C. Riemer, I. Iwasaki, *Corrosion* 43 (1986): p. 440-447.
44. C. Giovanni, W. Wang, S. Nowak, J.M. Greneche, H. Lecoq, L. Mouton, M. Giraud, C. Tard, *ACS Catal.* 4 (2014): p. 681-687.
45. E. Peters, "The Electrochemistry of Sulfide Minerals," in *Trends in Electrochemistry*, eds. J.O.M. Bockris, D.A.J. Rand, B.J. Welch (New York, NY: Plenum Press, 1977), p. 267-290.
46. P.R. Holmes, F.K. Crundwell, *Hydrometallurgy* 39 (1995): p. 353-375.
47. S.N. Esmaeely, B. Brown, S. Nešić, *Corrosion* 73 (2017): p. 144-154.
48. P. Jin, W. Robbins, G. Bota, *Corros. Sci.* 111 (2016): p. 822-834.
49. P. Jin, S. Nešić, *Corros. Sci.* 115 (2017): p. 93-105.
50. D. Barthelmy, "Pyrrhotite Mineral Data," Mineralogy Database, <http://webmineral.com/> (July 2, 2015).
51. R.G. Arnold, L.E. Reichen, *Am. Mineral.* 47 (1962): p. 105-111.
52. G.A. Desborough, R.H. Carpenter, *Econ. Geol.* 60 (1965): p. 1431-1450.
53. P. Chirita, J.D. Rimstidt, *Appl. Geochem.* 41 (2014): p. 1-10.
54. M.J. Nicol, P.D. Scott, *J. S. Afr. I. Min. Metall.* (1979): p. 298-305.
55. P.H. Tewari, A.B. Campbell, *Phys. Chem.* 80 (1976): p. 1844-1848.
56. M.P. Janzen, R.V. Nicholson, J.M. Scharer, *Geochim. Cosmochim. Acta* 64 (1999): p. 1511-1522.
57. P.H. Tewari, A.B. Campbell, *Can. J. Chem.* 57 (1979): p. 188-196.
58. P.H. Tewari, G. Wallace, A.B. Campbell, "The Solubility of Iron Sulfides and Their Role in Mass Transport in Groler-Sulfide Heavy Water Plants," Research Chemistry Branch, Whiteshell Nuclear Research Establishment, 1978, p. 5960.
59. A.V. Kuklinskii, Y.L. Mikhlin, G.L. Pashkov, V.F. Kargin, I.P. Asanov, *Russian J. Electrochem.* 37 (2001): p. 1269-1276.
60. J.E. Thomas, W.M. Skinner, R. St.C Smart, *Geochim. Cosmochim. Acta* 65 (2001): p. 1-12.
61. K.-L.J. Lee, "A Mechanistic Modeling of CO<sub>2</sub> Corrosion of Mild Steel in the Presence of H<sub>2</sub>S" (Ph.D. diss., Ohio University, 2004).
62. X. Jiang, Y.G. Zheng, D.R. Qu, W. Ke, *Corros. Sci.* 48 (2006): p. 3091-3108.
63. C.Q. Ren, X. Wang, L. Liu, H.E. Yang, N. Xian, *Mater. Corros.* 63 (2012): p. 168-172.
64. Z.F. Yin, W.Z. Zhao, Y.R. Feng, S.D. Zhu, *Corros. Eng. Sci. Technol.* 44 (2009): p. 453-461.
65. S. Navabzadeh Esmaeely, D. Young, B. Brown, S. Nešić, *Corrosion* 73 (2017): p. 238-246.
66. ASTM G1 (reapproved), "Standard Practice for Preparing, Cleaning, and Evaluating Corrosion Test" (West Conshohocken, PA: ASTM International, 2011).